Image Registration Guided Wavefield Tomography For Shear Wave Velocity Model Building

Di Yang, Xuefeng Shang, Alison Malcolm and Mike Fehler, MIT*

SUMMARY

Multi-component acquisitions offer the opportunity to form elastic migration images and to estimate elastic parameters of the subsurface. In this study, we propose an image registration guided S-wave velocity inversion method based on the knowledge of the P-wave velocities. The PS depth migration image is registered to the PP image with a shift function obtained by dynamic image warping. In each step, a target image is generated by warping the PS image by a fraction of the shift function to avoid cycle-skipping. Elastic image domain wavefield tomography is used to minimize the image differences between the PS image and the target image to update the S-wave velocities iteratively. The method works with high-frequency reflection data. Starting from an arbitrary constant S-wave velocity model, the inversion delivers a high quality PS image and a smooth velocity model.

INTRODUCTION

Multicomponent imaging methods that include converted phases have been proposed in the literature in both the time and depth domains. Herrenschmidt et al. (2001) investigated and compared several converted-wave imaging approaches with real data applications, and showed that prestack time migration provides interpretable results when lateral velocity variations are not significant. As with any imaging, prestack depth migration is preferred for complex velocity models. Kuo and Dai (1984) first proposed Kirchhoff elastic wave migration based on Kirchhoff-Helmholtz type integrals. Hokstad (2000) presented multicomponent Kirchhoff migration using the survey-sinking concept. Similar to acoustic Kirchhoff migration, these methods are likely to fail when ray-theory breaks down in complex media (Gray et al., 2001). One-wave migration methods can also be extended for elastic applications. Wapenaar and Haime (1990) propose to separate wave modes on the surface before one-way migration. Yan and Sava (2008) advocate an alternative procedure that uses the vector wavefields during propagation for reconstructing scalar and vector potentials and imaging using reverse time migration (RTM).

Although depth migration is capable of providing high-quality images, it also requires a reliable velocity model. A converted-wave migration velocity model is often obtained in the time domain by tuning the V_p/V_s ratio (Fomel et al., 2005; Hale, 2013). Assuming the P wave velocity is correct, the time shifts between PP and PS events can be transformed into V_p/V_s ratio corrections. Du et al. (2012a) propose a joint migration velocity analysis in the angle domain for both PP and PS depth images. However, Kirchoff based migration is used, which is likely to break down in complex structures. Yan and Sava (2010) present a wave-equation migration velocity (WEMVA) analysis method for shear wave velocity inversion based on elastic reverse time migration (ERTM) (Yan and Sava, 2008). It finds the S-wave velocities and PS depth migration images simultaneously, but this requires heavy computation, for calculating elastic extended images as well as angle decomposition, and does not take advantage of constraints from PP images.

Yang et al. (2014a) proposed an image domain wavefield tomography (IDWT) method for time-lapse velocity inversion based on the assumption that corresponding reflectors in time-lapse images should be at the same locations. A similar matching principle can be used for shear wave velocity inversion; such a principle states that reflectors in PS depth migrated images should be at the same depth as corresponding ones in PP depth migrated images. When the shear wave velocities are incorrect, we can measure and minimize the depth shifts between PS and PP images to recover the shear wave velocity model. The calculation of depth shifts can be achieved by image registration. Fomel and Backus (2003) introduces a least-squares optimization method for multicomponent data registration, but their method requires a good initial guess. The local similarity attribute is used for registering time-lapse images in Fomel and Jin (2009). Hale (2013) improves a dynamic programming method developed for speech recognition that computes time shifts in a robust and efficient manner, and applies it to registering PP and PS time migration images. Baek et al. (2014) present a robust piecewise polynomial dynamic time warping method with low-frequency augmented signals, and successfully combine it with full waveform inversion to mitigate cycle-skipping effects. All theses methods can potentially be applied for the registration of depth migrated images.

In this study, we propose a methodology for inverting S-wave velocities based on P-wave velocities by integrating image domain wavefield tomography (IDWT) (Yang et al., 2014a), dynamic image warping (DIW) (Hale, 2013) and the registration guided least-squares (RGLS) method (Baek et al., 2014). We first briefly describe the ERTM and DIW algorithms that are used in this study to form and register PS images, respectively. We then introduce the theory of elastic IDWT, and describe how we modify it using a RGLS framework. A three layer model is used to show how the method works.

THEORY

Elastic Reverse Time Migration

Reverse Time Migration (RTM) (Baysal et al., 1983; McMechan, 1983) is robust for imaging in complex geology. To form PP and PS images separately, the wave-modes should be separated during migration (Yan and Sava, 2008). Dellinger and Etgen (1990) propose separating the extrapolated wavefield into P and S potentials by applying the divergence and curl operators to the field $\mathbf{u}(\mathbf{x},t)$:

$$P = \nabla \cdot \mathbf{u}, \tag{1}$$

$$\mathbf{S} = \nabla \times \mathbf{u}. \tag{2}$$

DOI http://dx.doi.org/10.1190/segam2014-0847.1

For isotropic elastic media, the P mode is the compressional component of the wavefield propagating at speed V_p, and the **S** mode is the transverse component propagating at speed V_s. Because the **S** mode is a vector field, the imaging conditions for PS and SS images vary in how the vectors are treated. For example, a PS image can be obtained by applying

$$I_{PS} = \int_0^T P \cdot (\mathbf{I_3} \cdot \mathbf{S}) dt, \tag{3}$$

where $\mathbf{I_3}$ is the 3x3 identity matrix. Other imaging conditions (e.g., cross-correlating component by component (Yan and Sava, 2008)) can also be applied. The choice of imaging condition does not affect the generality of our framework. To simplify the discussion, we use Equation 3 for the following sections.

Dynamic Image Warping for Elastic Images

As described in Yang et al. (2014a) and Hale (2013), a migration image I made with an incorrect velocity can be considered a warped version of the true image $\widehat{I}$ made with the correct velocity. In Equation 4, $\mathbf{w}(\mathbf{x})$ is a vector warping function that specifies how much the image point at $\mathbf{x}$ in $\widehat{I}(\mathbf{x})$ is shifted from the same image point in $I(\mathbf{x})$,

$$I(\mathbf{x}) = \widehat{I}(\mathbf{x} + \mathbf{w}(\mathbf{x})). \tag{4}$$

Given $I(\mathbf{x})$ and $\widehat{I}(\mathbf{x})$, we can pose the optimization problem to solve for $\mathbf{w}(\mathbf{x})$ as:

$$\mathbf{w}(\mathbf{x}) = \arg\min_{\mathbf{l}(\mathbf{x})} D(\mathbf{l}(\mathbf{x})), \tag{5}$$

where

$$D(\mathbf{l}(\mathbf{x})) = \int_{\mathbf{x}} |\, I(\mathbf{x}) - \widehat{I}(\mathbf{x} + \mathbf{l}(\mathbf{x}))\, |^2 \, d\mathbf{x}. \tag{6}$$

Hale (2013) provides an efficient algorithm to solve similar problems for time warping with smooth constraints.

One issue that does require discussion is that in PS RTM images, the events with flipped polarity in the PS image will be mis-registered with the PP events. To mitigate this, we modify Equation 6 into

$$D(\mathbf{l}(\mathbf{x})) = \int_{\mathbf{x}} |\, I_{PP}(\mathbf{x}) - \Xi[I_{PS}(\mathbf{x} + \mathbf{l}(\mathbf{x}))]\, |^2 \, d\mathbf{x}, \tag{7}$$

where Ξ is an operator that corrects the polarities of the PS images. An efficient way to do this is to use poynting vectors following the method in Du et al. (2012b).

Elastic Image Domain Wavefield Tomography

Data domain inversion methods like full waveform inversion (Tarantola, 1984; Virieux and Operto, 2009), are designed to estimate model parameters by fitting observed data with simulated data. If we assume an observed image $I_{obs}(\mathbf{x})$ is available, a similar least-squares fitting cost function can be written

$$E(m) = \frac{1}{2} \sum_{x_s} \int_{\mathbf{x}} |I(\mathbf{x}, x_s, m) - I_{obs}(\mathbf{x}, x_s)|^2 d\mathbf{x}, \tag{8}$$

where I is the image we want to construct, $\mathbf{x}$ is the spatial vector, x_s is the source index and m is the velocity model to be recovered. Such methods are not commonly used for initial model building (e.g., WEMVA) because there are no observed images. Instead, velocity errors are characterized by the features of the events in image gathers, for example mis-focusing in time-lag gathers (Sava and Fomel, 2006; Yang and Sava, 2011) or flatness in angle gathers (Sava and Fomel, 2003; Yan and Sava, 2008).

In time-lapse situations, the observed image is available: the baseline image. The time-lapse velocity changes are estimated by fitting baseline images with monitor images (Yang et al., 2014b). In the context of S-wave velocity model building, the observed image is also available, if we have a reasonable P-wave velocity model. However, the PP image cannot be directly substituted into Equation 8 for several reasons. First, the PP and PS images generally have different wavelengths and amplitudes. Second, the PS image has zero values at normal incidence locations. Third, the PS and PP images from the same shot profile often have different migration apertures.

We thus require a way of estimating a modeled PS image from the PP image. This can be achieved by using the reflector locations in PP images to synthesize a target PS image $\widehat{I}_{PS}$. For this to work, we need to be able to match the reflectors in the two images so that we know which reflectors we need to synthesize the response from. This can be achieved efficiently by using image registration (Hale, 2013). Assuming that we obtain a spatial warping function $\mathbf{w}(\mathbf{x})$ from image registration which warps I_{PS} to I_{PP}, the cost function for S-wave velocity inversion can be written as:

$$E(\beta) = \frac{1}{2} \sum_{x_s} \int_{\mathbf{x}} |I_{PS}(\mathbf{x}, x_s, \beta) - \widehat{I}_{PS}(\mathbf{x}, x_s)|^2 d\mathbf{x}, \tag{9}$$

where $\widehat{I}_{PS}(\mathbf{x}, x_s) = I_{PS}(\mathbf{x} + \mathbf{w}(\mathbf{x}), x_s))$, and β is the S-wave velocity model. As we minimize the image differences in Equation 9, the PS images will have the same reflector locations as the PP image, and the S-wave velocity will be recovered.

We call the least-squares optimization problem in Equation 9 elastic image domain wavefield tomography (EIDWT). Similar to derivations for FWI and acoustic IDWT (Yang et al., 2014a), the formula for the gradient of $E(\beta)$ can be derived using the adjoint-state method (Plessix, 2006). We skip the lengthy derivation in this paper, and just present the final formula:

$$\frac{\partial E}{\partial \beta} = -\rho\beta \int_0^T \{[\nabla \lambda_{\mathbf{r}} + (\nabla \lambda_{\mathbf{r}})^T] : [\nabla \mathbf{u}_{\mathbf{r}} + (\nabla \mathbf{u}_{\mathbf{r}})^T]\} dt + 4\rho\beta \int_0^T (\nabla \cdot \lambda_{\mathbf{r}})(\nabla \cdot \mathbf{u}_{\mathbf{r}}) dt, \tag{10}$$

where $\cdot$ is the dot product and : is the Frobenius inner product. We denote by $\mathbf{u}_{\mathbf{r}}$ the back propagated receiver wavefield used to form RTM images; λ_r is the associated adjoint wavefield. This is obtained by solving the elastic wave equation

$$\rho \ddot{\lambda}_{\mathbf{r}} = \nabla \cdot (\mathbf{c} : \nabla \lambda_{\mathbf{r}}) + \mathscr{A}. \tag{11}$$

DOI http://dx.doi.org/10.1190/segam2014-0847.1

If we use the imaging condition in Equation 3, the adjoint source is:

$$\mathscr{A} = \nabla \times (\phi_I \mathbf{I_3}(\nabla \cdot \mathbf{u_s})), \quad (12)$$

where $\phi_I = I_{PS} - \widehat{I}_{PS}$, and $\mathbf{u_s}$ is the forward propagated source wavefield used to form the PS image.

Multi-level Optimization

This cost function in Equation 9 has the same drawback as the traditional FWI cost function. When reflector shifts are too large (> half wavelength, measured normal to the reflector), cycle skipping makes the cost function insensitive to local velocity perturbations. This is very likely to happen in S-wave velocity model building, especially when little prior information is available. Starting from an empirical V_p/V_s ratio might help, however, the convergence is still not guaranteed.

Baek et al. (2014) propose an RGLS method that uses a data domain cost function where the real data are substituted by fractionally warped data to make sure the synthetic waveforms are less than half a wavelength away from the true ones. Here we borrow this idea, and substitute a fractionally warped image I_{frac} for the fully warped image $\widehat{I}_{PS}$ in Equation 9 to avoid cycle-skipping. The fractionally warped image is defined as:

$$I_{frac} = I_{PS}(\mathbf{x} + \alpha \mathbf{w}(\mathbf{x})), \quad (13)$$

where $0 < \alpha \ll 1$, and $\mathbf{w}(\mathbf{x})$ is the original warping function. A sufficiently small α should be chosen to ensure that I_{frac} is close enough to I_{PS}.

Now we can write the registration guided EIDWT (RG-EIDWT) method as the following multi-level optimization problem. Given the current S-wave velocity model β_k after iteration k,

(i) We use DIW to solve Equation 5 for the warping function $\mathbf{w}(\mathbf{x})$ that registers the current I_{PS} to I_{PP};

(ii) We fractionally warp I_{PS} to I_{frac} with $\alpha \mathbf{w}(\mathbf{x})$, and use EIDWT to minimize

$$E(\beta_{k+1}) = \frac{1}{2} \sum_{x_s} \int_{\mathbf{x}} |I_{PS}(\mathbf{x}, x_s, \beta_{k+1}) - I_{frac}(\mathbf{x}, x_s)|^2 d\mathbf{x}, \quad (14)$$

to recover β_{k+1} iteratively;

(iii) We go back to step (i), adjust α, and repeat step (ii).

In the process above, the overall image shift between the original I_{PS} and I_{PP} is minimized fraction by fraction. The parameter α determines the size of each fraction; this choice could also be optimized to expedite the overall convergence. To avoid cycle-skipping, the safest choice for α should satisfy $max(\alpha \mathbf{w}(\mathbf{x})) = d/2$, where d is the normal spatial wavelength of the reflectors in I_{PS}. Because d varies with the S-wave velocity, further optimization can be achieved by using an $\alpha(\mathbf{x})$ that is a function of space. In this paper, we use a single-valued α to simply the process.

SYNTHETIC EXAMPLE

Figure 1 shows the true P- and S-wave velocity models used in this test. Eight sources are placed on the surface evenly spaced at an interval of 300 m. We use 300 receivers with a 10 m spacing, also on the surface, to cover the entire model. Synthetic datasets are generated by an elastic finite difference solver. The source wavelet is a standard Ricker wavelet centered at 15 Hz. Both x-components and z-components of the waves are collected.

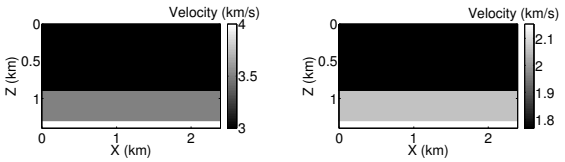

Figure 1: (a) True P-wave velocity model. (b) True S-wave velocity model. The S-wave velocities in three layers are 1767, 2060 and 2150 m/s respectively.

We assume that through velocity model building, a smooth version of the P-wave velocity model is available and sufficient for migration. Instead of assigning an empirical V_p/V_s ratio, we use a constant 1900 m/s S-wave velocity model as the starting model (Figure 2(a)). We perform ERTM beginning from the smooth P and constant S velocity models. In Figure 2(b), we piece the P-P and P-S images together to show the depth mismatch of the reflectors. The left half is the P-P image, and the right half is the P-S image. Both are formed by stacking the RTM images of all the shots. Because the constant S-wave velocity is higher than the true velocity in the first layer (1767 m/s), the first reflector in the P-S image is shifted downward by about half a wavelength. The S-wave velocity of the second layer is higher than 1900 m/s, so the second reflector is shifted a little less.

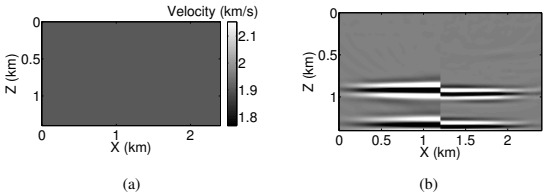

Figure 2: (a) Starting model with constant S-wave velocity 1900 m/s. (b) Comparison between PP (left half) and PS (right half) images. Both images are formed with all 8 sources.

Figure 3(a) shows the PS image produced with one shot gather. The black star marks the location of the shot. To register this image with the PP image, the polarity of the reflectors to the left of the shot is corrected. DIW calculates the warping function in Figure 3(b) that shows the maximum depth shift of the PS image to be 70 m. To form I_{frac} in Equation 13, we need to use the original PS image without polarity correction as shown in Figure 4(a). We multiply the warping function by $\alpha = 0.5$, and use it to warp Figure 4(a) towards the reflectors in the PP image. Figure 4(b) presents a zoom of the reflectors (dashed line in Figure 4(a)). The blue wiggles, that are the warped reflectors, are shifted upwards from the red ones (original im-

DOI http://dx.doi.org/10.1190/segam2014-0847.1

age). The subtraction between the red and blue images generates the ϕ_I in Equation 12 to form the adjoint sources.

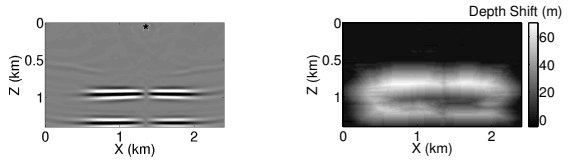

Figure 3: (a) The polarity-corrected PS image formed with one shot gather. Black star marks the location of the source. (b) The warping function calculated by DIW. It describes how much the depth shift is for each image point in the PS image in (a)

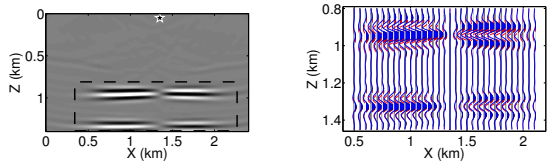

Figure 4: (a) Original PS image without polarity correction. The same source is used as in Figure 3(a). (b) The zoom-in view of the reflectors marked by black dashed line in (a). The original image (red wiggles) and the fractionally warped image (blue wiggles) are shown together.

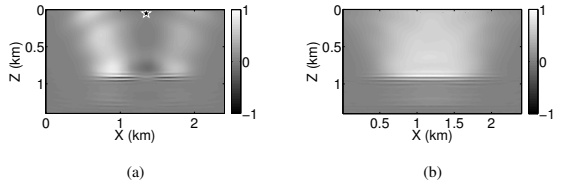

Figure 5: (a) The gradient for the source marked by the black star. Dominant energy is along the receiver wave-path. (b) Total gradient by stacking partial gradients from each source.

Figure 5(a) shows the gradient calculated with the adjoint sources. The dominant energy is on the wave-paths from the adjoint sources to the receivers. This is because only the shear wavefield from the receivers is used to form the PS image. As a result, the perturbation of the PS image is only sensitive to the S-wave velocities along the S-wave propagation paths in the receiver field. Since the P-wave velocity is correct, there is no energy on the source-side wave-path. By summing the gradients from all of the shots, we obtain the total gradient in Figure 4(b) used to update the velocity model. The positive values in the gradient indicate that the current velocity is generally too high.

After 20 iterations, we obtain the final S-wave velocity model as shown in Figure 6(a). Both the low velocity (1757 m/s) in the first layer and the high velocity (2060 m/s) in the second

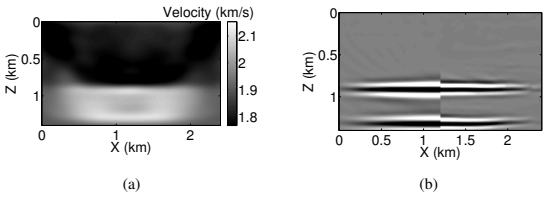

Figure 6: (a). The recovered S-wave velocity model after 20 iterations. Both the low and high velocity layers are resolved. (b). The PS image formed with the recovered S-wave velocity model in (a) is compared with the PP image.

layer are recovered. The third layer still has the starting velocity because there is no reflection from below. On the edges of the model, the recovery is poorer particularly for deeper regions, due to illumination limits. We plot 1D vertical velocity profiles at the center of the true, inverted and starting S-wave velocity models in Figure 7 to show the recovery. We compare the final PS image with the PP image in Figure 6(b). It is obvious that the reflectors in the P-S image (right half) are aligned with those in the P-P image (left half). The alignment is also not as good on the edges due to the same illumination limits. We expect the recovery to be improved with a wider acquisition surface.

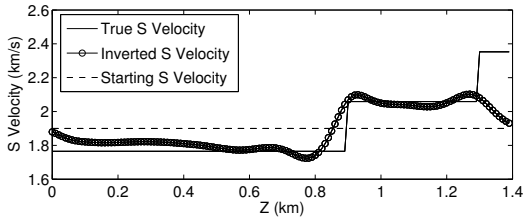

Figure 7: 1D vertical velocity profile at the center of the S models.

CONCLUSION

We have proposed an image registration guided wavefield tomography method in the image domain for S-wave velocity model building with the knowledge of P-wave velocities. The shifts of the PS images with respect to the PP image are minimized fraction by fraction to recover the S-wave velocities iteratively. The method is full wavefield based and makes no assumptions about the smoothness of the subsurface. It works well with high-frequency reflection data, and can start with an arbitrary constant S-wave velocity model. It is computationally efficient, without requiring the calculation of angle gathers or extended images. We have shown a synthetic model in which the interval velocities are successfully recovered.

ACKNOWLEDGMENTS

This work was supported by the MIT Earth Resources Laboratory Founding Members Consortium.

DOI http://dx.doi.org/10.1190/segam2014-0847.1

http://dx.doi.org/10.1190/segam2014-0847.1

EDITED REFERENCES

Note: This reference list is a copy-edited version of the reference list submitted by the author. Reference lists for the 2014 SEG Technical Program Expanded Abstracts have been copy edited so that references provided with the online metadata for each paper will achieve a high degree of linking to cited sources that appear on the Web.

REFERENCES

Baek, H., H. Calandra, and L. Demanet, 2014, Velocity estimation via registration-guided least-squares inversion: Geophysics, **79**, no. 2, R79–R89, http://dx.doi.org/10.1190/geo2013-0146.1.

Baysal, E., D. D. Kosloff, and J. W. C. Sherwood, 1983, Reverse-time migration: Geophysics, **48**, 1514–1524, http://dx.doi.org/10.1190/1.1441434.

Dellinger, J., and J. Etgen, 1990, Wavefield separation in two-dimensional anisotropic media : Geophysics, **55**, 914–919, http://dx.doi.org/10.1190/1.1442906.

Du, Q., F. Li, J. Ba, Y. Zhu, and B. Hou, 2012a, Multicomponent joint migration velocity analysis in the angle domain for PP-waves and PS-waves: Geophysics, **77**, no. 1, U1–U13, http://dx.doi.org/10.1190/geo2010-0423.1.

Du, Q., Y. Zhu, and J. Ba, 2012b, Polarity reversal correction for elastic reverse time migration: Geophysics, **77**, no. 2, S31–S41, http://dx.doi.org/10.1190/geo2011-0348.1.

Fomel, S., and M. Backus, 2003, Multicomponent seismic data registration by least squares: 73rd Annual International Meeting, SEG, Expanded Abstracts, 781–784.

Fomel, S., M. Backus, K. Fouad, B. Hardage, and G. Winters, 2005, A multistep approach to multicomponent seismic image registration with application to a West Texas carbonate reservoir study: 75th Annual International Meeting, SEG, Expanded Abstracts, 1018–1021, http://dx.doi.org/10.1190/1.2147852.

Fomel, S., and L. Jin, 2009, Time-lapse image registration using the local similarity attribute: Geophysics, **74**, no. 2, A7–A11, http://dx.doi.org/10.1190/1.3054136.

Gray, S., J. Etgen, J. Dellinger, and D. Whitmore, 2001, Seismic migration problems and solutions: Geophysics, **66**, 1622–1640, http://dx.doi.org/10.1190/1.1487107.

Hale, D., 2013, Dynamic warping of seismic images: Geophysics, **78**, no. 2, S105–S115, http://dx.doi.org/10.1190/geo2012-0327.1

Herrenschmidt, A., P.-Y. Granger, F. Audebert, C. Gerea, G. Etienne, A. Stopin, M. Alerini, S. Lebegat, G. Lambaré, P. Berthet, S. Nebieridze, and J.-L. Boelle, 2001, Comparison of different strategies for velocity model building and imaging of PP- and PS-real data: The Leading Edge, **20**, 984–995, http://dx.doi.org/10.1190/1.1487320.

Hokstad, K., 2000, Multicomponent Kirchhoff migration: Geophysics, **65**, 861–873, http://dx.doi.org/10.1190/1.1444783.

Kuo, J., and T. Dai, 1984, Kirchhoff elastic wave migration for the case of noncoincident source and receiver: Geophysics, **49**, 1223–1238, http://dx.doi.org/10.1190/1.1441751.

McMechan, G. A., 1983, Migration by extrapolation of time-dependent boundary values: Geophysical Prospecting, **31**, no. 3, 413–420, http://dx.doi.org/10.1111/j.1365-2478.1983.tb01060.x.

Plessix, R.-E., 2006, A review of the adjoint-state method for computing the gradient of a functional with geophysical applications: Geophysical Journal International, **167**, no. 2, 495–503, http://dx.doi.org/10.1111/j.1365-246X.2006.02978.x.

Sava, P., and S. Fomel, 2003, Angle-domain common-image gathers by wavefield continuation methods: Geophysics, **68**, 1065–1074, http://dx.doi.org/10.1190/1.1581078.

Sava, P., and S. Fomel, 2006, Time-shift imaging condition in seismic migration: Geophysics, **71**, no. 6, S209–S217, http://dx.doi.org/10.1190/1.2338824.

Tarantola, A., 1984, Inversion of seismic reflection data in the acoustic approximation: Geophysics, **49**, 1259–1266, http://dx.doi.org/10.1190/1.1441754.

Virieux, J., and S. Operto, 2009, An overview of full-waveform inversion in exploration geophysics: Geophysics, **74**, no. 6, WCC1–WCC26, http://dx.doi.org/10.1190/1.3238367.

Wapenaar, C. P. A., and G. C. Haime, 1990, Elastic extrapolation of primary seismic P- and S-waves: Geophysical Prospecting, **38**, no. 1, 23–60, http://dx.doi.org/10.1111/j.1365-2478.1990.tb01833.x.

Yan, J., and P. Sava, 2008, Isotropic angle-domain elastic reverse-time migration: Geophysics, **73**, no. 6, S229–S239, http://dx.doi.org/10.1190/1.2981241.

Yan, J., and P. Sava, 2010, Analysis of converted-wave extended images for migration velocity analysis: 80th Annual International Meeting, SEG, Expanded Abstracts, 1666–1671, http://dx.doi.org/10.1190/1.3513161.

Yang, D., A. Malcolm, and M. Fehler, 2014a, Using image warping for time-lapse image domain wavefield tomography: Geophysics, **79**, no. 3, WA141–WA151, http://dx.doi.org/10.1190/geo2013-0424.1.

Yang, D., A. Malcolm, M. Fehler, and L. Huang, 2014b, Timelapse walkaway vertical seismic profile monitoring for CO_2 injection at the SACROC enhanced oil recovery field: A case study: Geophysics, **79**, no. 2, B51–B61, http://dx.doi.org/10.1190/geo2013-0274.1.

Yang, T., and P. Sava, 2011, Wave-equation migration velocity analysis with time-shift imaging: Geophysical Prospecting, **59**, no. 4, 635–650, http://dx.doi.org/10.1111/j.1365-2478.2011.00954.x.